ACS APPLIED MATERIALS & INTERFACES

Letter

www.acsami.org

Formation of He-Rich Layers Observed by Neutron Reflectometry in the He-Ion-Irradiated Cr/W Multilayers: Effects of Cr/W Interfaces on the He-Trapping Behavior

Feida Chen,[†] Xiaobin Tang,[*,†,‡] Hai Huang,[†] Xinxi Li,[§] Yan Wang,[§] Chaoqiang Huang,[§] Jian Liu,[†] Huan Li,[†] and Da Chen[†,‡]

[†]Department of Nuclear Science & Engineering, Nanjing University of Aeronautics and Astronautics, Nanjing 211106, China

[‡]Jiangsu Key Laboratory of Nuclear Energy Equipment Materials Engineering, Nanjing 211106, China

[§]Institute of Nuclear Physics and Chemistry, China Academy of Engineering Physics, Mianyang 621900, China

ABSTRACT: Cr/W multilayer nanocomposites were presented in the paper as potential candidate materials for the plasma facing components in fusion reactors. We used neutron reflectometry to measure the depth profile of helium in the multienergy He ions irradiated $[Cr/W\ (50\ nm)]_3$ multilayers. Results showed that He-rich layers with low neutron scattering potential energy form at the Cr/W interfaces, which is in great agreement with previous modeling results of other multilayers. This phenomenon provided a strong evidence for the He trapping effects of Cr/W interfaces and implied the possibility of using the Cr/W multilayer nanocomposites as great He-tolerant plasma facing materials.

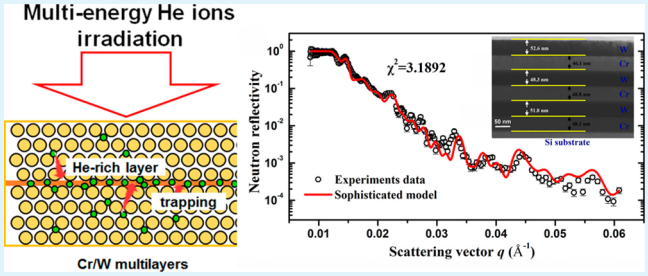

KEYWORDS: *Cr/W multilayer, He ion irradiation, neutron reflectometry, interfaces, trapping behavior*

1. INTRODUCTION

Tungsten and its alloys have a high melting point, low vapor pressure, high temperature strength, and high energy threshold for surface sputtering.[1,2] These properties make tungsten alloys among the most attractive candidate materials for plasma-facing components (PFCs) in fusion reactors, such as the divertor armor tiles, the outer vertical target, the dome, and the cassette body.[3−6] However, after being long-term exposed to the relevant radiation conditions of fusion reactors, the tungsten alloys generate abundant helium (He) atoms either directly from the plasma or from the transmutation reactions induced by neutrons.[7−9] Previous researches on fusion materials have identified the problem of accumulation of He atoms, which induces bubbles, cracks, surface exfoliation, erosion, and embrittlement, all of which seriously degrade the physical and mechanical properties of tungsten alloys.[10−14]

One approach proposed in the past decade to controlling the deleterious effects of He in alloys is the utilization of high-density grain boundaries and hetero interfaces in materials as He atoms sinks to delay the nucleation and growth of He bubbles. Considering these needs, M. J. Demkowicz and A. Misra et al. designed the Cu/Nb multilayer nanocomposites with thermal stable interfaces and presented the experimental evidence that He bubbles growth can be arrested by hetero interfaces between the immiscible Cu/Nb sublayers.[15−17] Presently, we report a new kind of composites of tungsten with a nanoscale multilayer structure, which is composed of the immiscible Cr and W, and investigate the effects of Cr/W interfaces on the He trapping behaviors by neutron reflectometry. The Cr/W interface is remarkably stable under the high energy Xe ions irradiation, and exhibits excellent inhibiting effect against radiation induced swelling and grain growth in our previous work.[18] Because the He−V clusters smaller than 1 nm in diameter are barely observable by transmission electron microscopy (TEM), even when using the under-focus model,[19] we characterized the concentration profiles of He across the Cr/W interfaces via neutron reflectometry, which has high sensitivity to He and possesses subangstrom level resolution of depth.[20]

2. EXPERIMENTAL METHOD

In this work, the Cr/W multilayer nanocomposite samples were deposited on 2 mm thick single crystal Si substrates by RF magnetron sputtering, as described in ref 17. As shown in Figure 1c, the total thickness of the multilayer thin films was about 300 nm, and each single Cr and W layers was approximately 50 nm thick (referred to as $[Cr/W\ (50\ nm)]_3$ in the subsequent paragraphs). Room temperature He ions implantation experiments using three different energies were then performed on the 320 kV platform at the Institute of Modern Physics, Chinese Academy of Sciences to produce a uniform depth profile of He atoms in the Cr/W multilayers. The fluence of the 12, 30, and 50 keV He ions was $0.73 \times 10^{16}/cm^2$, $1.46 \times 10^{16}/cm^2$, and $2.19 \times 10^{16}/cm^2$, respectively. The total He depth profile calculated using SRIM2013[21] is shown in Figure 1b.

Received: June 19, 2016
Accepted: September 2, 2016
Published: September 2, 2016

DOI: 10.1021/acsami.6b07419
ACS Appl. Mater. Interfaces 2016, 8, 24300−24305

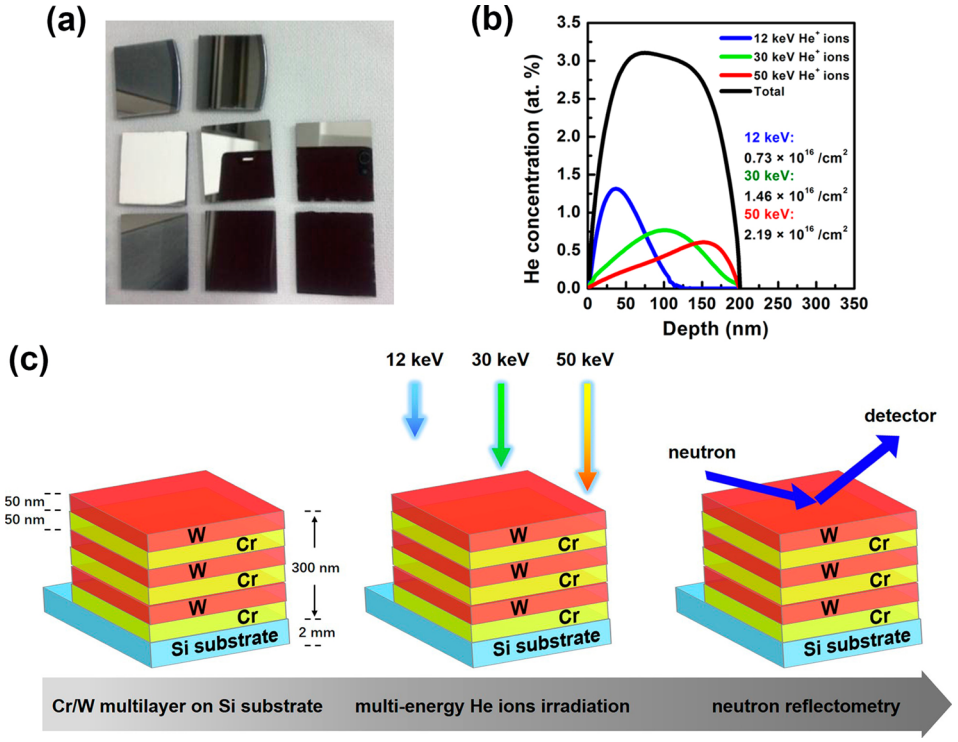

Figure 1. (a) Photo of the Cr/W multilayers on the Si substrate, (b) He depth profile in the irradiated $[Cr/W\ (50\ nm)]_3$ multilayer calculated using SRIM. The final He concentration within a depth range of 50 to 150 nm is well-distributed around 3.0 at %. (c) Schematic illustration of the neutron reflection measurements of the multienergy He-irradiated $[Cr/W\ (50\ nm)]_3$ multilayers.

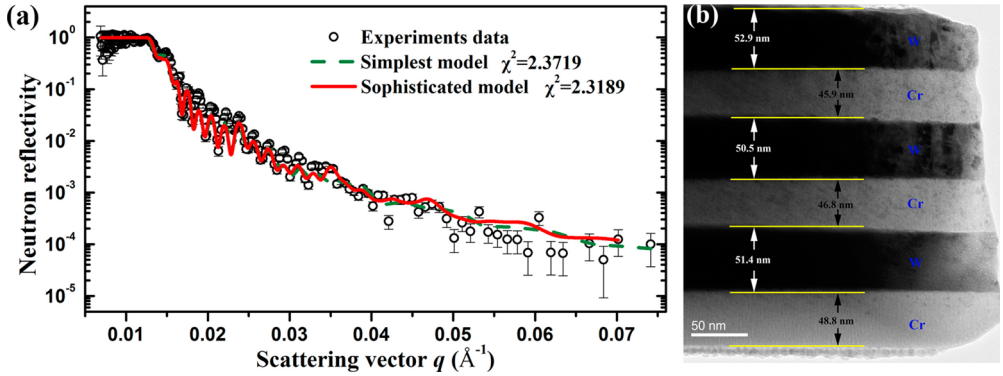

Figure 2. (a) Neutron reflectivity data achieved by the experiments and the best-fitting curves of the as-deposited $[Cr/W\ (50\ nm)]_3$ multilayer nanocomposites. The fitting degree is 2.3719 for the simplest model and 2.3189 for the sophisticated model, (b) TEM cross-section image of the as-deposited $[Cr/W\ (50\ nm)]_3$ multilayer nanocomposites. The thickness of each sublayer is 52.9, 45.9, 50.5, 46.8, 51.4, and 48.8 nm.

After He ion irradiation experiments, the neutron reflectometry measurements on the multilayer samples were performed on the time of flight polarized neutron reflectometer (TPNR) at the Key Laboratory of Neutron Physics, China Academy of Engineering Physics.[22] The neutron reflectometry curves were measured as a function of the scattering vector q, which is entirely determined by the incident angle of the neutron beam and the incident neutron wavelength

$$q = \frac{4\pi}{\lambda}\sin\theta \tag{1}$$

where λ is the incident neutron wavelength and θ is the angle between the incident neutron beam and the sample surface. In our experiments, the incident angle θ was kept constant and neutron wavelength λ was varied. It was realized by using a cold neutron beam with different energy from the reactor. The traveling time of the neutron beam from the chopper to detector was measured. The wavelength of each neutron in the beam can be calculated according to the traveling time and then we can get the reflectometry curve. On the TPNR setup at the Key Laboratory of Neutron Physics, the neutron wavelength range varies from 2.5 to12.5 Å. We utilized two different neutron incident angles (0.5 and 0.9°) and combined the two reflectivity curves to generate the final data to cover the entire range of q (0.007 to 0.07 $Å^{-1}$). Subsection point of q in the combined curve was 0.016 $Å^{-1}$. Neutron wavelength resolution and angular resolution in the experiments were 0.081 Å and 0.11 mrad, respectively.

3. RESULTS AND DISCUSSION

Figure 2a shows the neutron reflectivity data and fitting curves of the as-deposited $[Cr/W\ (50\ nm)]_3$ multilayer nanocomposites. The fitting was performed using PNR_Multilayer, a neutron reflectivity data fitting software developed at China Academy of Engineering Physics. First, it calculates the reflection wave amplitude in the $[Cr/W\ (50\ nm)]_3$ multilayer according to the preset structure parameters of the multilayer

DOI: 10.1021/acsami.6b07419
ACS Appl. Mater. Interfaces 2016, 8, 24300−24305

Table 1. Best-Fitted Structure Parameters of Two Models of the As-Deposited Cr/W Multilayer

simplest model				sophisticated model			
layer	element	thickness (Å)	scattering potential energy (neV)	layer	element	thickness (Å)	scattering potential energy (neV)
				1	C	14.6	102.52
1	W	513.06	82.13	2	W	537.95	83.87
2	Cr	472.14	95.1	3	Cr	472.14	95.1
3	W	511.29	82.13	4	W	501.61	83.87
4	Cr	473.77	95.1	5	Cr	460.58	95.1
5	W	506.93	82.13	6	W	511.44	83.87
6	Cr	484.74	95.1	7	Cr	484.74	95.1
7	SiO_2	19.35	95	8	SiO_2	20	95
8	Si substrate	∞	54	9	Si substrate	∞	54

model by using the Parratt's recursion formula. Then, it calculates the deviation between the fitting curve and experiment data, and adjusts the structure parameters of the model to reduce the deviation by using the genetic algorithm. After fitting, we deduced the neutron scattering potential energy depth profile of the $[Cr/W\ (50\ nm)]_3$ multilayer sample, which is shown in Table 1.

The deduction of the neutron scattering potential energy depth profile from the reflectivity measurements is a well-known inverse problem of neutron reflectometry. If the sample is a single layer film, only 4 unknown parameters need to be deduced: layer thickness, neutron scattering potential energy, neutron absorption coefficient, and the interface roughness. The deduction is simple and accurate. But if the sample is a multilayer film, number of the structure parameters to be determined increase with the layer number of multilayer film proportionally. Thus, unless the limits of these parameters are set according to the known information from the initial design, Transmission Electron Microscope (TEM) images or other measurement results, there will be an infinite number of different neutron scattering potential energy depth profiles resulting in the same reflectivity curve.

To reconstruct the elements depth profile of the as-deposited $[Cr/W\ (50\ nm)]_3$ multilayer nanocomposites sample in our work, first we build a simplest model with three Cr/W bilayers placed on a Si substrate (surface of Si substrate covered with a thin layer of SiO_2). As shown in Figure 2b, the thicknesses of the six metal sublayers and the SiO_2 thin layer are 52.9 nm, 45.9 nm, 50.5 nm, 46.8 nm, 51.4 nm 48.8 nm, and 1 nm according to the TEM measurements. We used them as the initial thicknesses of the preset model. Considering the measurement error and thickness of interface region, we allowed that the thickness of each layer vary within ±5 nm away from the preset value during the optimization procedure. And for the neutron scattering potential energy, one can calculate it as follows

$$V = 26.04\mathrm{SLD} \tag{2}$$

$$\mathrm{SLD} = \sum_{i=1}^{k} n_i b_i \tag{3}$$

where V is the neutron scattering potential energy (unit is neV), SLD is the neutron scattering length density (unit is $Å^{-2}$), n_i is the atomic density of the ith nuclide, and b_i is the coherent scattering length of the ith nuclide. The coherent scattering lengths of Cr, W, Si, C, O and He are 3.635 fm, 4.86 fm, 4.1491 fm, 6.646 fm, 5.803 fm and 3.26 fm, respectively.[23] Hence the neutron scattering potential energies of pure W and Cr are calculated to be 80.2 neV and 78.9 neV according to eqs 2 and 3. Given that the oxygen adsorption or oxidation phenomenon may exist in the metallic layers, the potential energy value of W and Cr layers was allowed to vary from 80.2 neV (W) to 84 neV (W with oxygen adsorption) and from 78.9 neV (Cr) to 95.1 neV (Cr_2O_3) during the optimization procedure. To simplify the fitting process, we assumed the neutron scattering potential energies of three Cr/W bilayers are the same. Furthermore, as the neutron absorption effects is weak and the interface roughness mainly affects the larger q region of the curve according to the Nevot − Croce factor,[24] their influences on the shape of the reflectivity curve are very slight. Since we do not know the possible range of the interface roughness and a few nanometer's measurement error in thickness of each layer is acceptable in this work (because the main purpose of this work focused on the change of neutron scattering potential energies on the interfaces), the neutron absorption coefficient and the interface roughness were approximated as zero in the fitting model to improve the efficiency of fitting. Thus, there were 9 parameters with limits need to be determined in the model.

Moreover, we also took into account a more sophisticated model which includes an adhesion layer forms on the surface constitutes from hydrocarbons and water. For simplicity, we assumed that the adhesion layer consists of carbon only. Since the carbon layer is loose, its density is less than 1.26 g/cm^3.[25] Thus, the initial neutron scattering potential energies of this layer were set to 109.39 neV according to eq 2 and 3. The optimized structure parameters of this model is also listed in Table 1.

As shown in Table 1, the difference between the optimized structure parameters of the two models from neutron reflectometry is not significant. Both of them coincide with the TEM cross-section image of the as-deposited Cr/W sample very well. Meanwhile, as shown in Figure 2(a), the dash curve stands for the simplest model and the solid curve stands for the more sophisticated model. The fitting degrees of the two curves are very close. The critical points of total reflection of the two curves are both at 0.012 $Å^{-1}$, while the position of each interference peaks in the fitting curves also coincide with the experimental data. This result indicates that the uniformity of the as-deposited multilayer sample is great and validates the compatibility of our multilayer model. According to the fitting result of the sophisticated model, the neutron scattering potential energy of the Cr sublayer is 95.1 neV, which is the theoretical value of Cr_2O_3. By contrast, the neutron scattering potential energy of the W sublayer is 83.87 neV, which is slightly larger than the theoretical value of pure W (80.2 neV). From this point of view, the oxygen adsorption or oxidation phenomenon exists in the Cr and W sublayers.

DOI: 10.1021/acsami.6b07419
ACS Appl. Mater. Interfaces 2016, 8, 24300−24305

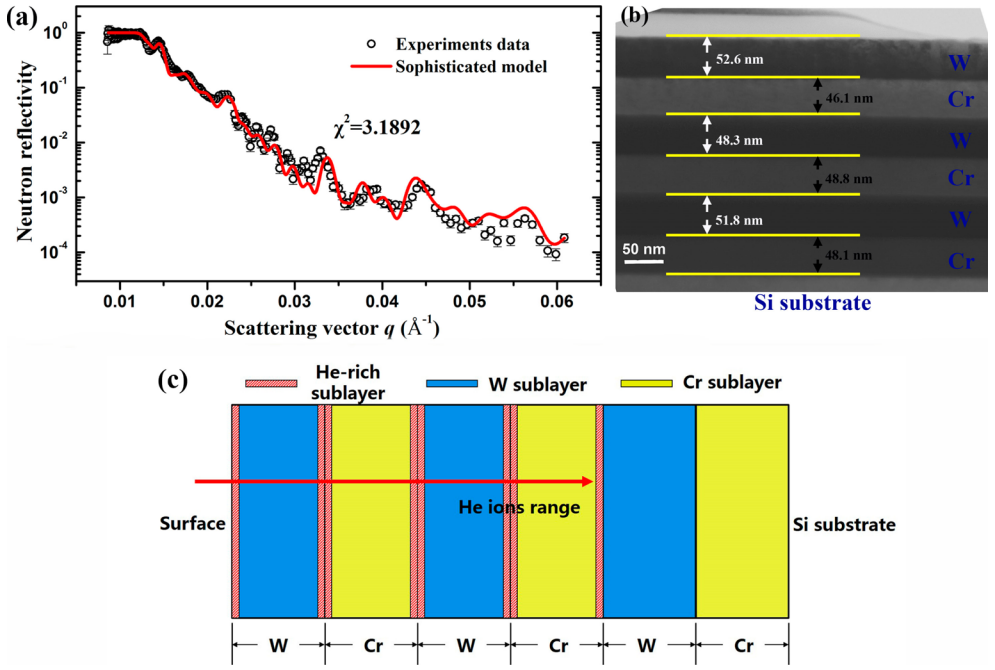

Figure 3. (a) Neutron reflectivity data achieved by the experiments and the best-fitting curve of the postirradiated $[Cr/W\ (50\ nm)]_3$ multilayer nanocomposites. The fitting degree is 3.6152. (b) TEM cross-section image of the postirradiated $[Cr/W\ (50\ nm)]_3$ multilayer nanocomposites. The thickness of each sublayer is 52.6, 46.1, 48.3, 48.8, 51.8, and 48.1 nm. (c) He-rich sublayers distribution in the He-ion-irradiated Cr/W multilayer nanocomposites.

The deduction was also performed on the postirradiated $[Cr/W\ (50\ nm)]_3$ multilayer nanocomposites. Figure 3 shows the neutron reflectivity curve and the TEM cross-section image of the postirradiated $[Cr/W\ (50\ nm)]_3$ multilayer nanocomposites. Although no conspicuous He bubbles or other changes could be observed from the TEM image shown in Figure 3b, obvious differences can be observed between the neutron reflectivity curves of the as-deposited (shown in Figure 2a) and postirradiated Cr/W multilayers (shown in Figure 3a). According to the He depth profile calculation result of SRIM, if neglecting the diffusion behavior of helium atoms, then the He concentration of the second and third sublayers should be well-distributed at approximately 3 at %, whereas the fifth and sixth sublayers are unaffected by the He atoms. Thus, the model used previously may also be suitable for this case. However, the fitting result under this model could not achieve good convergence with the experimental data, which strongly indicates that the diffusion of He atoms plays an important role in the final He depth profile, making the He concentration in each sublayer inhomogeneous. To reflect the inhomogeneous inside the sublayers, it is necessary to divide each sublayer to thinner layers to study the depth profile of the neutron scattering potential energy. Hence, we increased the number of sublayer of our preset model to make it closer to the inhomogeneous He distribution in the postirradiated sample. The details of the optimizing model are listed in Table 2, and the fitting curve is shown in Figure 3a as a red line, which fits well with the experimental data.

As shown in Table 2, new layers with low neutron scattering potential energy form at the Cr/W interfaces of the first four sublayers of the postirradiated $[Cr/W\ (50\ nm)]_3$ multilayer. As calculated by SRIM, the maximum He concentration is approximately 3 at. %, at the depth range from 50 to 150 nm. Assuming that the formation of these low neutron scattering potential energy sublayers is due to the enrichment of He atoms at the interfaces, the neutron scattering potential energy of the W sublayer combined with the maximum He decreases from 80.2 neV to 79.42 neV, whereas the potential energy of the Cr sublayer combined with the maximum He decreases from 95.1 neV to 67.31 neV. The best-fitted neutron scattering potential energies listed in Table 2 coincide with this hypothesis, and then potential energy gradually return to normal levels as depth increases. Meanwhile, the total thickness of each adjacent three layers (namely, Cr−He layer, Cr layer and Cr−He layer) coincides with the thickness observed from the TEM measurements shown in Figure 3b, which supports the validity of the deduction. Figure 3c illustrates the

Table 2. Best-Fitted Structure Parameters of the Sophisticated Model of the He-Ion-Irradiated Cr/W Multilayer

layer	element	thickness (Å)	scattering potential energy (neV)
1	C	10	100.476
2	W−He	51.59	79.13
3	W	382.54	83.87
4	W−He	79.37	77.06
5	Cr−He	187.42	50.18
6	Cr	164.96	95.1
7	Cr−He	45.67	78.3
8	W−He	96.85	62.4
9	W	382.35	83.53
10	W−He	42.52	72.6
11	Cr−He	167.46	51.77
12	Cr	258.73	94.44
13	Cr−He	23.23	70.69
14	W	517.42	79.77
15	Cr	477.77	94.2
16	SiO_2	18.53	95
17	Si substrate	∞	54

DOI: 10.1021/acsami.6b07419
ACS Appl. Mater. Interfaces 2016, 8, 24300−24305

distribution of the He-rich sublayers in the Cr/W multilayer concluded by the neutron reflectivity fitting result of the postirradiated sample.

In the previous studies, the multilayer nanocomposites irradiated by large fluences of He ions at high temperature were observed to form finely dispersed, 1−2 nm diameter He bubbles, instead of He bubbles larger than 20 nm diameter in the bulk region.[26] Atomic simulation studies indicated that the interaction between He atoms and the interface was responsible for the suppressing of He bubble growth.[16] Using neutron reflectometry, we found that the He concentration at the Cr/W interfaces is significantly higher than the estimate of SRIM, even at room temperature. As illustrated in Figure 4, given that

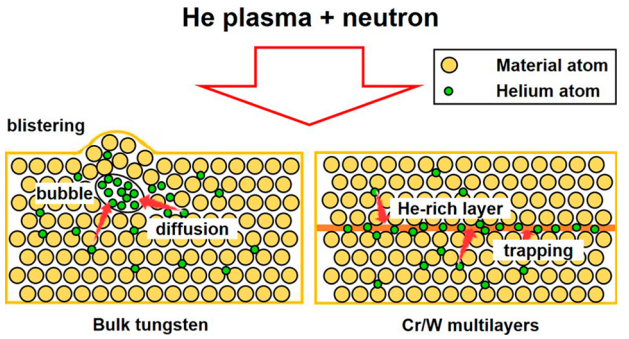

Figure 4. Illustration of the He trapping effects of Cr/W interface on the inhibition of He bubble formation.

He atoms diffused toward the Cr/W interfaces to form He-rich layer, He concentration in the bulk region decreased observably, which leads to the enhanced He tolerant performance of Cr/W multilayers. This phenomenon is in great agreement with the previous studies on the formation of the void-denuded zones (VDZs) near grain boundaries.[27] Notably, the measurement result of neutron reflectometry is statistically significant, as the counts are averaged over the entire sample area (3.5 cm × 3.5 cm).

4. CONCLUSION

In conclusion, a new kind of Cr/W multilayer nanocomposites was presented as a potential candidate material for the PFC in fusion reactors. The Cr/W interfaces were proven to be effective sinks for He atoms by neutron reflectometry. With the movement of He atoms toward the Cr/W interfaces, He concentration in the bulk region decreases below the critical concentration for He bubbles growth, thereby enhancing the He tolerance of the Cr/W multilayer nanocomposites.

AUTHOR INFORMATION

Corresponding Author

*E-mail: tangxiaobin@nuaa.edu.cn.

Notes

The authors declare no competing financial interest.

ACKNOWLEDGMENTS

We thank Jingyu Li, Huiping Liu, Long Kang, and Tongmin Zhang for help during the ion irradiation experiments. The irradiation experimental work was performed on the 320 kV platform for multidiscipline research, with highly charged ions at the Institute of Modern Physics, CAS. This work was funded by the Priority Academic Program Development of Jiangsu Higher Education Institutions, the Fundamental Research Funds for the Central Universities (Grant No. NJ20150021).

REFERENCES

(1) Jiang, D. Y.; Ouyang, C. Y.; Liu, S. Q. The Effect of Titanium Doping on Carbon Behavior in Tungsten: A First-Principles Study. *Fusion Eng. Des.* **2016**, *112*, 123−129.

(2) Giusepponi, S.; Celino, M. The Effects of Vacancies in the Mechanical Properties of Tungsten: A First-Principles Study. *Nucl. Instrum. Methods Phys. Res., Sect. B* **2015**, *342*, 70−75.

(3) Zinkle, S. J.; Busby, J. T. Structural Materials for Fission & Fusion Energy. *Mater. Today* **2009**, *12* (11), 12−19.

(4) Missirlian, M.; Bucalossi, J.; Corre, Y.; Ferlay, F.; Firdaouss, M.; Garin, P.; Grosman, A.; Guilhem, D.; Gunn, J.; Languille, P.; Lipa, M.; Richou, M.; Tsitrone, E. The WEST Project: Current Status of the ITER-like Tungsten Divertor. *Fusion Eng. Des.* **2014**, *89* (7−8), 1048−1053.

(5) Fernandez, N.; Ferro, Y.; Kato, D. Hydrogen Diffusion and Vacancies Formation in Tungsten: Density Functional Theory Calculations and Statistical Models. *Acta Mater.* **2015**, *94*, 307−318.

(6) Wang, S. M.; Sun, C. X.; Guo, W. H.; Yan, Q. Z.; Zhou, Z. J.; Zhang, Y. C.; Shen, W. P.; Ge, C. C. Review on the Explosive Consolidation Methods to Fabricate Tungsten based PFMs. *J. Nucl. Mater.* **2014**, *455* (1−3), 174−179.

(7) de Broglie, I.; Beck, C. E.; Liu, W.; Hofmann, F. Temperature Dependence of Helium-Implantation-Induced Lattice Swelling in Polycrystalline Tungsten: X-ray Micro-Diffraction and Eigenstrain Modelling. *Scr. Mater.* **2015**, *107*, 96−99.

(8) Hasegawa, A.; Fukuda, M.; Nogami, S.; Yabuuchi, K. Neutron Irradiation Effects on Tungsten Materials. *Fusion Eng. Des.* **2014**, *89* (7−8), 1568−1572.

(9) Chen, F. D.; Tang, X. B.; Yang, Y. H.; Huang, H.; Liu, J.; Chen, D. Characterization of Neutron Induced Damage Effect in Several Types of Metallic Multilayer Nanocomposites based on Monte Carlo Simulation. *Nucl. Instrum. Methods Phys. Res., Sect. B* **2015**, *358*, 88−92.

(10) Iyyakkunnel, S.; Marot, L.; Eren, B.; Steiner, R.; Moser, L.; Mathys, D.; Duggelin, M.; Chapon, P.; Meyer, E. Morphological Changes of Tungsten Surfaces by Low-Flux Helium Plasma Treatment and Helium Incorporation via Magnetron Sputtering. *ACS Appl. Mater. Interfaces* **2014**, *6* (14), 11609−11616.

(11) El-Atwani, O.; Hinks, J. A.; Greaves, G.; Gonderman, S.; Qiu, T.; Efe, M.; Allain, J. P. In-situ TEM Observation of the Response of Ultrafine- and Nanocrystalline-Grained Tungsten to Extreme Irradiation Environments. *Sci. Rep.* **2014**, *4*, 4716.

(12) Parish, C. M.; Hijazi, H.; Meyer, H. M.; Meyer, F. W. Effect of Tungsten Crystallographic Orientation on He-Ion-Induced Surface Morphology Changes. *Acta Mater.* **2014**, *62*, 173−181.

(13) Baldwin, M. J.; Doerner, R. P. Helium Induced Nanoscopic Morphology on Tungsten under Fusion Relevant Plasma Conditions. *Nucl. Fusion* **2008**, *48* (3), 035001.

(14) Becquart, C. S.; Domain, C. Migration Energy of He in W Revisited by ab Initio Calculations. *Phys. Rev. Lett.* **2006**, *97* (19), 196402.

(15) Han, W. Z.; Demkowicz, M. J.; Mara, N. A.; Fu, E. G.; Sinha, S.; Rollett, A. D.; Wang, Y. Q.; Carpenter, J. S.; Beyerlein, I. J.; Misra, A. Design of Radiation Tolerant Materials via Interface Engineering. *Adv. Mater.* **2013**, *25* (48), 6975−6979.

(16) Demkowicz, M. J.; Misra, A.; Caro, A. The Role of Interface Structure in Controlling High Helium Concentrations. *Curr. Opin. Solid State Mater. Sci.* **2012**, *16* (3), 101−108.

(17) Kashinath, A.; Misra, A.; Demkowicz, M. J. Stable Storage of Helium in Nanoscale Platelets at Semicoherent Interfaces. *Phys. Rev. Lett.* **2013**, *110* (8), 086101.

(18) Chen, F. D.; Tang, X. B.; Huang, H.; Liu, J.; Li, H.; Qiu, Y. L.; Chen, D. Surface Damage and Mechanical Properties Degradation of Cr/W Multilayer Films Irradiated by Xe^{20+}. *Appl. Surf. Sci.* **2015**, *357*, 1225−1230.

(19) Zhang, H. X.; Ren, F.; Wang, Y. Q.; Hong, M. Q.; Xiao, X. H.; Qin, W. J.; Jiang, C. Z. In situ TEM Observation of Helium Bubble

DOI: 10.1021/acsami.6b07419
ACS Appl. Mater. Interfaces 2016, 8, 24300−24305

Evolution in V/Ag Multilayer During Annealing. *J. Nucl. Mater.* **2015**, *467* (2), 537−543.
(20) Zhernenkov, M.; Jablin, M. S.; Misra, A.; Nastasi, M.; Wang, Y. Q.; Demkowicz, M. J.; Baldwin, J. K.; Majewski, J. Trapping of Implanted He at Cu/Nb Interfaces Measured by Neutron Reflectometry. *Appl. Phys. Lett.* **2011**, *98* (24), 241913.
(21) Ziegler, J. F.; Ziegler, M. D.; Biersack, J. P. SRIM − The Stopping and Range of Ions in Matter. *Nucl. Instrum. Methods Phys. Res., Sect. B* **2010**, *268* (11−12), 1818−1823.
(22) Li, X. X.; Wang, Y.; Huang, C. Q.; Chen, B. Design and Simulation of Time-of-Flight Neutron Reflectometer. *Nucl. Sci. Technol.* **2010**, *21* (3), 157−160.
(23) Sears, V. F. Neutron Scattering Lengths and Cross Sections. *Neutron News* **1992**, *3* (3), 26−37.
(24) Nevot, L.; Croce, P. Caractérisation des Surfaces par Réflexion Rasante de Rayons X. Application à L'étude du Polissage de Quelques Verres Silicates. *Rev. Phys. Appl.* **1980**, *15* (3), 761−779.
(25) Filatova, E. O.; Kozhevnikov, I. V.; Sokolov, A. A.; Ubyivovk, E. V.; Yulin, S.; Gorgoi, M.; Schafers, F. Soft X-Ray Reflectometry, Hard X-Ray Photoelectron Spectroscopy and Transmission Electron Microscopy Investigations of the Internal Structure of TiO_2(Ti)/SiO_2/Si Stacks. *Sci. Technol. Adv. Mater.* **2012**, *13*, 015001.
(26) Hattar, K.; Demkowicz, M. J.; Misra, A.; Robertson, I. M.; Hoagland, R. G. Arrest of He Bubble Growth in Cu−Nb Multilayer Nanocomposites. *Scr. Mater.* **2008**, *58*, 541−544.
(27) Han, W. Z.; Demkowicz, M. J.; Fu, E. G.; Wang, Y. Q.; Misra, A. Effect of Grain Goundary Character on Sink Efficiency. *Acta Mater.* **2012**, *60*, 6341−6351.

DOI: 10.1021/acsami.6b07419
ACS Appl. Mater. Interfaces 2016, 8, 24300−24305